



**HAL**  
open science

# Gravity waves in the middle atmosphere during the MaCWAVE winter campaign: evidence of mountain wave critical level encounters

L. Wang, D. C. Fritts, B. P. Williams, R. A. Goldberg, F. J. Schmidlin, U. Blum

► **To cite this version:**

L. Wang, D. C. Fritts, B. P. Williams, R. A. Goldberg, F. J. Schmidlin, et al.. Gravity waves in the middle atmosphere during the MaCWAVE winter campaign: evidence of mountain wave critical level encounters. *Annales Geophysicae*, 2006, 24 (4), pp.1209-1226. hal-00318035

**HAL Id: hal-00318035**

**<https://hal.science/hal-00318035>**

Submitted on 18 Jun 2008

**HAL** is a multi-disciplinary open access archive for the deposit and dissemination of scientific research documents, whether they are published or not. The documents may come from teaching and research institutions in France or abroad, or from public or private research centers.

L'archive ouverte pluridisciplinaire **HAL**, est destinée au dépôt et à la diffusion de documents scientifiques de niveau recherche, publiés ou non, émanant des établissements d'enseignement et de recherche français ou étrangers, des laboratoires publics ou privés.

# Gravity waves in the middle atmosphere during the MaCWAVE winter campaign: evidence of mountain wave critical level encounters

L. Wang<sup>1</sup>, D. C. Fritts<sup>1</sup>, B. P. Williams<sup>1</sup>, R. A. Goldberg<sup>2</sup>, F. J. Schmidlin<sup>3</sup>, and U. Blum<sup>4</sup>

<sup>1</sup>NorthWest Research Associates, Inc., Colorado Res. Associates Division, 3380, Mitchell Lane Boulder, CO 80301, USA

<sup>2</sup>NASA/Goddard Space Flight Center, Greenbelt, Maryland, USA

<sup>3</sup>NASA/GSFC/Wallops Flight Facility, Wallops Island, Virginia, USA

<sup>4</sup>Forsvarets forskningsinstitutt, NO-2027 Kjeller, Norway

Received: 13 September 2005 – Revised: 24 January 2006 – Accepted: 13 February 2006 – Published: 3 July 2006

Part of Special Issue “MaCWAVE: a rocket-lidar-radar program to study the polar mesosphere during summer and winter”

**Abstract.** Falling sphere and balloon wind and temperature data from the MaCWAVE winter campaign, which was conducted in northern Scandinavia during January 2003, are analyzed to investigate gravity wave characteristics in the stratosphere and mesosphere. There were two stratospheric warming events occurring during the campaign, one having a maximum temperature perturbation at ~45 km during 17–19 January, and the other having a maximum perturbation at ~30 km during 24–27 January. The former was a major event, whereas the latter was a minor one. Both warmings were accompanied by upper mesospheric coolings, and during the second warming, the upper mesospheric cooling propagated downward. Falling sphere data from the two salvos on 24–25 January and 28 January were analyzed for gravity wave characteristics. Gravity wave perturbations maximized at ~45–50 km, with a secondary maximum at ~60 km during Salvo 1; for Salvo 2, wave activity was most pronounced at ~60 km and above.

Gravity wave horizontal propagation directions are estimated using the conventional hodographic analysis combined with the S-transform (a Gaussian wavelet analysis method). The results are compared with those from a Stokes analysis. They agree in general, though the former appears to provide better estimates for some cases, likely due to the capability of the S-transform to obtain robust estimates of wave amplitudes and phase differences between different fields.

For Salvo 1 at ~60 km and above, gravity waves propagated towards the southeast, whereas for Salvo 2 at similar altitudes, waves propagated predominantly towards the northwest or west. These waves were found not to be to-

pographic waves. Gravity wave motions at ~45–50 km in Salvo 1 were more complicated, but they generally had large amplitudes, short vertical scales, and their hodographs revealed a northwest-southeast orientation. In addition, the ratios between wave amplitudes and intrinsic phase speeds generally displayed a marked peak at ~45–50 km and decreased sharply at ~50 km, where the background winds were very weak. These results suggest that these wave motions were most likely topographic waves approaching their critical levels. Waves were more nearly isotropic in the lower stratosphere.

**Keywords.** Meteorology and atmospheric dynamics (Middle atmosphere dynamics; Waves and tides; Turbulence)

## 1 Introduction

Atmospheric gravity waves (GWs) and their dissipation associated with wave saturation have long been recognized to play an important role in the large-scale circulation and the temperature and constituent structures of the middle atmosphere. For example, the zonal-mean forces associated with GW dissipation are believed to cause the closure of the mesospheric jets and a mean meridional circulation that leads to a warm winter mesopause, a cold summer mesopause, and a reversal of the latitudinal temperature gradient than would have been expected from an atmosphere in radiative equilibrium (e.g., Houghton, 1978; Lindzen, 1981; Holton, 1982); GWs contribute to driving the tropical quasi-biennial oscillation (QBO) (e.g., Dunkerton, 1997) and semiannual oscillation (SAO) in both the stratosphere and mesosphere (e.g., Hitchman et al., 1992); topographic wave drag is believed to

Correspondence to: L. Wang  
(lwang@cora.nwra.com)

slow the westerly winds above the midlatitude tropospheric jet maximum and significantly affect the northern winter climate (e.g., Palmer et al., 1986; McFarlane, 1987); they also play a role in driving the summer hemisphere meridional transport circulation (e.g., Alexander and Rosenlof, 1996) expressed through the downward control principle, and contribute to the formation of the winter stratospheric polar vortex (e.g., Hitchman et al., 1989). The interested readers are referred to Fritts (1984) and Fritts and Alexander (2003) for extensive reviews of the history and our current understanding of GW dynamics and their effects in the atmosphere. As noted in Fritts and Alexander (2003), observational and theoretical studies have also revealed considerable temporal and geographic variability of the GW source spectrum and its effects in the middle atmosphere. To date, however, our knowledge about the spatial and temporal variations of GW sources is still very limited, and more detailed observations are needed to characterize and quantify GW sources and their effects on the atmosphere at greater altitudes.

With the aim to study GW forcing of the polar mesosphere and lower thermosphere (MLT) region, two MaCWAVE (Mountain and Convective Waves Ascending Vertically) collaborative rocket and ground-based measurement campaigns were performed in northern Scandinavia (Goldberg et al., 2003, 2004, 2006). The summer component, which was coordinated closely with the MIDAS (Middle Atmosphere Dynamics and Structure) rocket program, was performed at the Andoya Rocket Range, Norway (69.3° N, 16.1° E) and the nearby ALOMAR observatory during July 2002 and has been described in detail in Goldberg et al. (2004) and Becker and Fritts (2006). Briefly, the mean state structure and GW activity from the troposphere to the mesosphere were characterized (Goldberg et al., 2004; Schöch et al., 2004; Rapp et al., 2004; Williams et al., 2004). It was found that there was a warmer mesopause, a colder middle mesosphere, and thus a more stable temperature gradient in the upper mesosphere during July 2002 than observed during previous summers. Meanwhile, the mean meridional circulation was markedly weaker near the mesopause than previous years. The unusual mean circulation and thermal structure were found to be consistent with the GW characteristics measured (Becker et al., 2004; Becker and Fritts, 2006).

The winter MaCWAVE rocket campaign in January 2003 was moved to ESRANGE, Sweden (67.9° N, 21.1° E), which is located on the east side (or lee) of the Scandinavian mountains. The rocket measurements were also supplemented by coordinated satellite and ground-based measurements at both ESRANGE and Andoya. Northern Scandinavia has been found to be a preferred site for penetration of mountain waves into the middle atmosphere in winter, and several independent campaigns have already examined the influences of the Scandinavian mountain ridge on GWs and polar stratospheric cloud formation (e.g., Dörnbrack et al., 2002; Blum et al., 2005; Eckermann et al., 2006). GWs excited by topography, or mountain waves, have phase speeds near zero,

so critical levels occur where the background wind is zero in the direction of wave propagation. A significant stratospheric warming immediately prior to our winter measurement program led to a reversal of the zonal wind, which prevented the penetration of mountain waves into the mesosphere. Nevertheless, there existed clear GW perturbations, some of which appear to be clear indications of mountain wave critical level encounters, with GW motions at higher altitudes due to sources other than topography.

Our goal in this study is to investigate in detail GW characteristics in the stratosphere and mesosphere employing data collected during the winter MaCWAVE rocket program. Because this campaign occurred during a major stratospheric warming, a major focus is on the behavior of apparent mountain waves approaching their critical levels. We employ both conventional and wavelet methods to assess GW structure in the stratosphere and mesosphere.

The paper is organized as follows. Section 2 describes the falling sphere and other data used in this study. Section 3 describes the mean state structure during the winter campaign and the estimation of GW perturbations. Section 4 introduces a new approach to derive GW horizontal propagation directions and analyzes GW characteristics for the pronounced signals identified in the falling sphere data. A discussion of the results is given in Sect. 5, and our summary and conclusion are presented in Sect. 6.

## 2 Data

During the MaCWAVE winter campaign, 35 Viper and Super-Loki rockets were launched successfully from ESRANGE, Sweden (67.9° N, 21.1° E) during 15–30 January 2003 to obtain falling sphere horizontal wind and temperature measurements throughout much of the middle atmosphere (35–90 km). The details of the rocket launches are provided by Goldberg et al. (2006). The details of the falling sphere instrumentation have been described in Schmidlin et al. (1991) and Williams et al. (2004). Briefly, the horizontal winds were determined from falling sphere positions which were tracked by a mobile, high-precision, C-band tracking radar. The temperature was related to the atmospheric density assuming hydrostatic equilibrium, while the density was determined from the falling sphere's vertical acceleration also tracked by the C-band radar. The vertical resolution of falling sphere (FS) measurements decreased with increasing altitude. It was ~6 km at 80 km, and ~30 m at ~35–40 km (note that the vertical profile of the Nyquist vertical wavelength corresponding to the FS data, which is twice the vertical resolution and is computed from the FS smoothing function, is shown in Fig. 6 below). Below 80 km, the accuracy of winds at the resolved scales was ~1 ms<sup>-1</sup>, whereas that of temperature was ~1 K. Above 80 km, the accuracy of both winds and temperature was generally poorer. As a result, we will focus in this study on analyzing GW characteristics below 80 km.

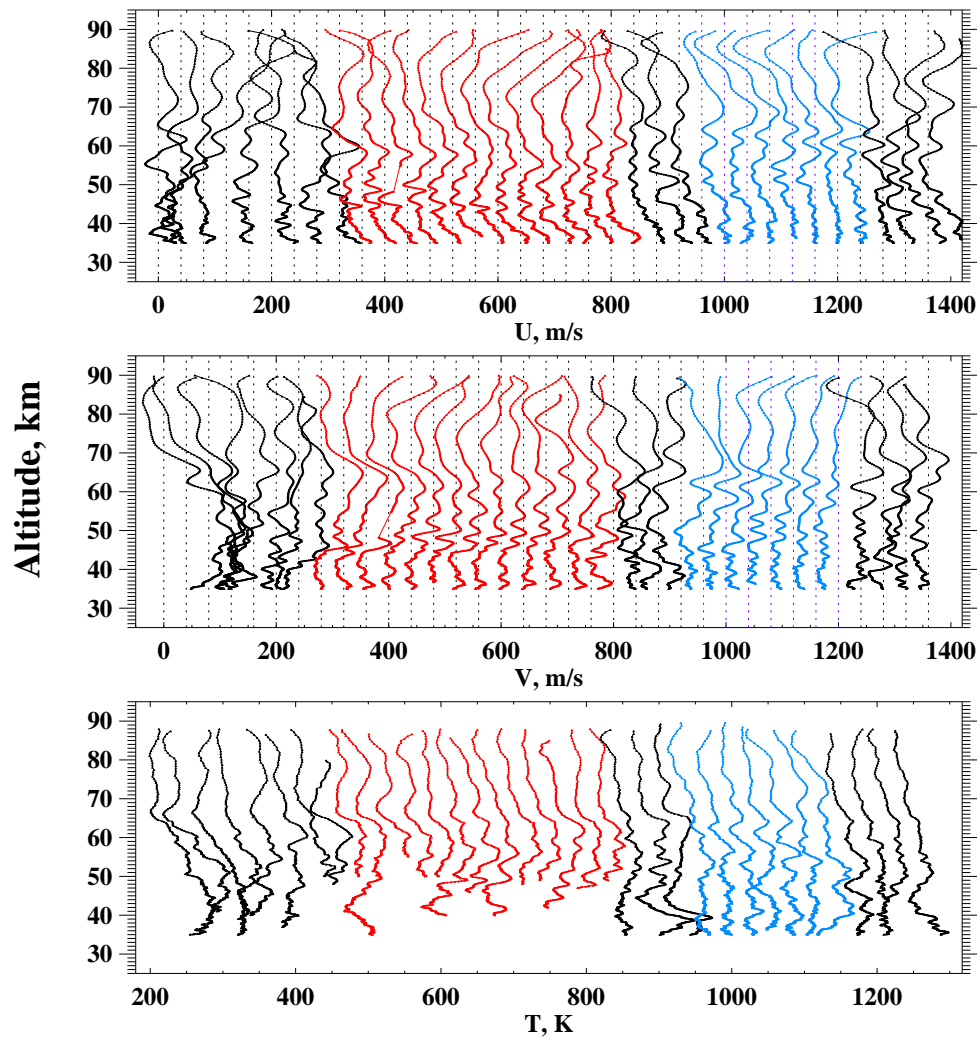


**Fig. 1.** Waterfall plots of falling sphere zonal and meridional winds (the upper two panels) and temperature raw soundings (the lower panel) over ESRANGE, Sweden ( $67.9^{\circ}$  N,  $21.1^{\circ}$  E) during the MaCWAVE winter campaign. Soundings in Salvo 1 are marked in red, whereas those in Salvo 2 are marked in blue. The horizontal spacing of adjacent profiles is  $40 \text{ ms}^{-1}$  for winds and  $30 \text{ K}$  for temperature. Temporally adjacent profiles are plotted with equal spacing regardless of the actual time difference. The temporal resolution of the soundings was generally 1 or 2 days, except during Salvo 1 and 2, for which the resolution was  $\sim 1\text{h}$ .

Figure 1 shows waterfall plots of the raw FS wind and temperature soundings during the winter campaign. As described in detail by Goldberg et al. (2006), the temporal resolution of the soundings was generally 1 or 2 days, except during Salvos 1 and 2 (which are shown in red and blue colors in Fig. 1, respectively), for which the resolution was  $\sim 1\text{h}$ . More detailed information on the soundings can be found in Goldberg et al. (2006). There were 13 soundings in Salvo 1 on 24–25 January and 7 soundings in Salvo 2 on 28 January. The good spatial and temporal resolution and extent within each salvo made it possible to obtain reliable estimates of the background fields and to extract credible GW perturbations. Hence, we will focus on analyzing GW characteristics for soundings within the two salvos in this study.

Note that wavelike structures are clearly seen in the waterfall plots. It is also apparent that wave perturbations were largest at  $\sim 45\text{--}50 \text{ km}$  for Salvo 1, although there were also clear wave motions at  $\sim 60 \text{ km}$ . Wave motions were most pronounced at  $\sim 60 \text{ km}$  for Salvo 2. In general, wind measurements reached lower altitudes than temperature. This is because drag (and temperature) could not be estimated accurately when the falling sphere collapsed and became non-spherical. However, this did not impact wind estimates.

The FS measurements were found to be consistent with observations from other collaborative instruments. These include temperatures from the U. Bonn lidar at ESRANGE (Blum and Fricke, 2005) and the SABER instrument (e.g., Mertens et al., 2004) onboard the TIMED satellite (during the days

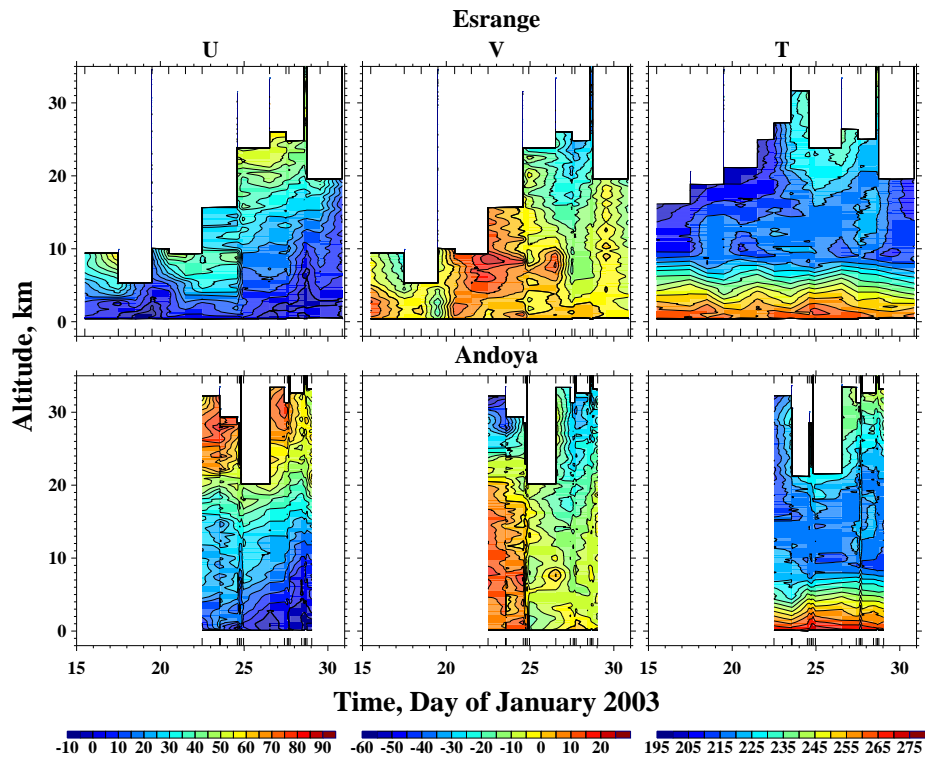


**Fig. 2.** Time-altitude contours of radiosonde measurements of winds and temperature over Esrange, Sweden ( $67.9^{\circ}$  N,  $21.1^{\circ}$  E) and Andoya, Norway ( $69.3^{\circ}$  N,  $16.0^{\circ}$  E). The contour interval is  $10 \text{ ms}^{-1}$  for winds and  $10 \text{ K}$  for temperature. The time coordinates corresponding to individual soundings are marked by the inward ticks. In the abscissa, the outward tick corresponding to each day indicates the beginning of that day.

when the SABER field of view passed Esrange) and winds from the meteor radar and sodium lidar above  $80 \text{ km}$  over Esrange and ALOMAR (not shown).

In addition to FS measurements, there were horizontal wind and temperature observations from 17 GPS MARK II meteorological radiosondes (having  $10\text{-s}$  resolution) released over Esrange, and from 19 radiosondes released over Andoya, Norway ( $69.3^{\circ}$  N,  $16.0^{\circ}$  E), which is  $\sim 200 \text{ km}$  from Esrange upwind of the Scandinavia Mountains. The temperature accuracy of the radiosonde was  $0.2 \text{ K}$ . The accuracy of winds was variable but was generally better than  $1 \text{ ms}^{-1}$ . The vertical resolution of the balloon measurements was  $\sim 40\text{--}60 \text{ m}$ . Figure 2 shows the time-altitude contours of raw radiosonde observations of horizontal winds and temperature over the two stations. The inward ticks on the plots show the release time of each sounding. The temporal resolution of the balloon soundings was variable, and there were no corresponding groups of balloon soundings over Esrange that matched the two FS salvos closely in time. In fact, there were only two balloon soundings available, which were close in time to each of the FS salvos. Most of the balloons burst below  $35 \text{ km}$ , and the bursting height was generally lower at Esrange than at Andoya. For the few soundings reaching  $35 \text{ km}$ , the wind and temperature profiles were found to agree

well with those of the FS in the overlapping altitude range (not shown). The altitudes reached for wind measurements were not always the same as those of temperature, as seen in Fig. 2. This is because temperatures were obtained by radiosondes, whereas winds were retrieved from the balloon positions, and these could occasionally not be obtained reliably due to low elevation angles. We note also that balloon data over both stations provided evidence of the stratospheric warming on 24 January.

In the next section, we will describe the mean state during the campaign, the background winds and temperature of the two FS salvos, and the extraction of GW perturbations.

### 3 Background fields and gravity wave perturbations

Before proceeding with our GW analysis, we wish to provide an overview of the background winds and temperature during the period of the observations. Figure 3 shows the merged time-altitude contours of zonal and meridional winds and temperature from FS (above  $35 \text{ km}$ ) and ECMWF T106 analyses (below  $35 \text{ km}$ ). To obtain the contours, we first interpolated the FS raw data, as shown in Fig. 1, to a regular altitude grid with a vertical resolution of  $0.2 \text{ km}$  (the same altitude grid was used for the salvo means and GW perturbations

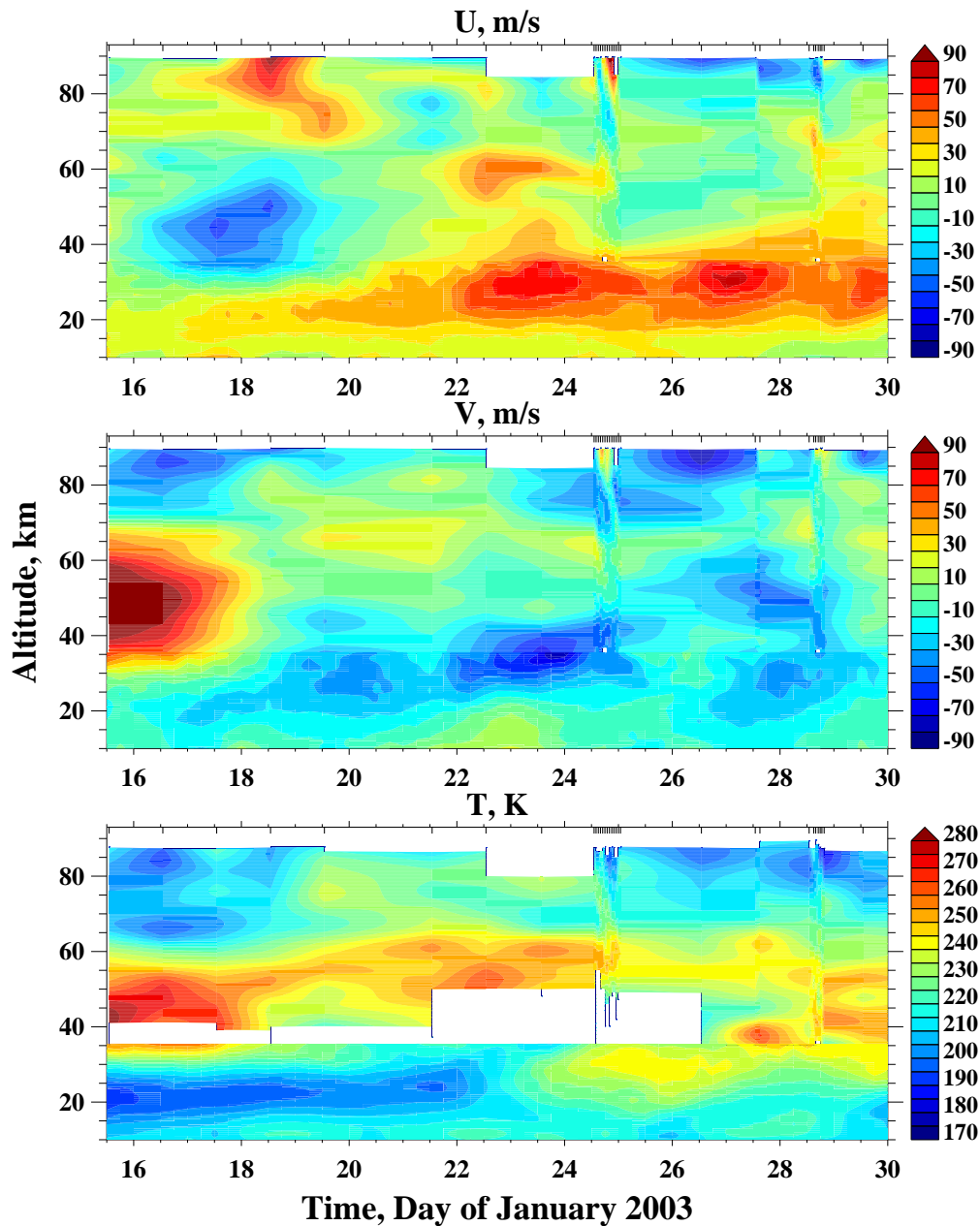


**Fig. 3.** Merged time-altitude contours of zonal and meridional winds and temperature from falling sphere (above 35 km) and ECMWF T106 four times daily analyses (below 35 km). The contour interval is  $10 \text{ ms}^{-1}$  for winds and 5 K for temperature. The inward ticks on the top of each panel indicate the actual times of the falling sphere soundings.

to be described later in this section), then smoothed each profile using a 5-km low-pass filter. The time corresponding to each FS sounding is indicated by the inward ticks at the top of each panel in Fig. 3. The ECMWF data plotted were the ECMWF T106 4 times daily analyses at  $68.625^\circ \text{ N}$ ,  $20.250^\circ \text{ E}$ . The balloon data (Fig. 2) were not used in the merged plot due to its limited altitude coverage over Esrange, though the balloon data and ECMWF analyses generally agreed very well when and where they overlapped, as

can be seen from comparing Figs. 2 and 3. The tropospheric information was excluded from Fig. 3 to focus on the stratospheric and mesospheric fields. Note that FS observations and ECMWF analyses generally merged very well.

There was evidence of a stratospheric warming occurring at  $\sim 45 \text{ km}$  on 15–17 January. The same structure was also observed with the U. Bonn lidar (Blum et al., 2006). There was further evidence of a warming, occurring at  $\sim 30 \text{ km}$  on 24–27 January, which was also detected

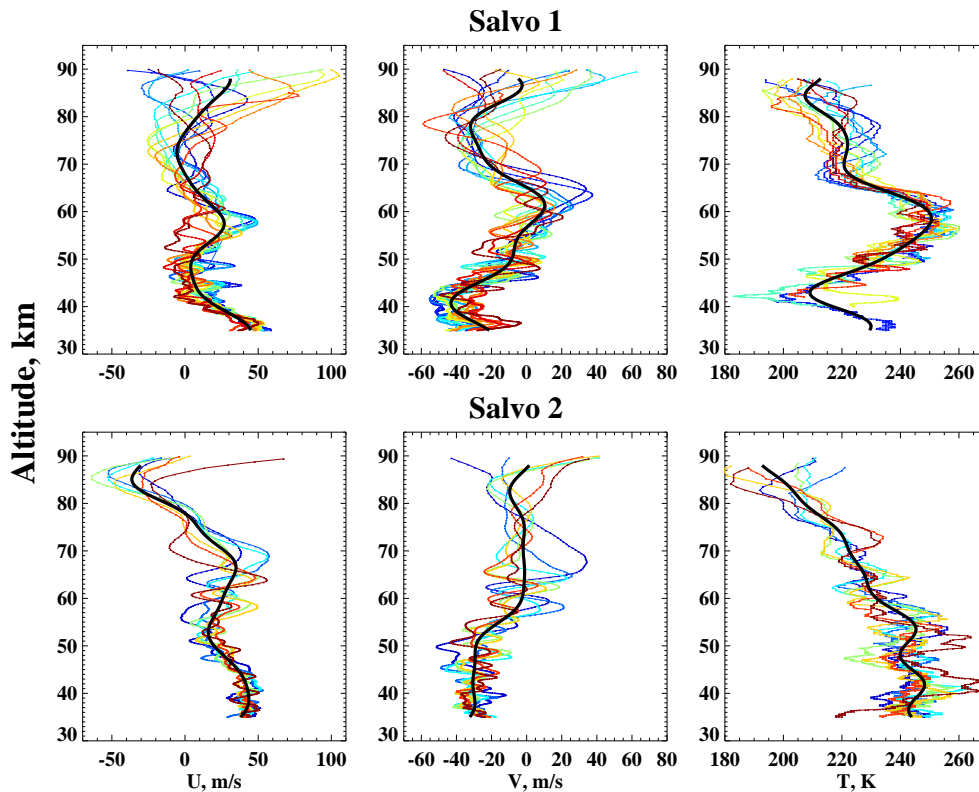


**Fig. 4.** Salvo mean winds and temperature (the thick dark lines) and the individual soundings within each salvo (the thin colored lines, with blue colors indicating earlier soundings and red colors indicating later soundings).

in the balloon soundings (Fig. 2). These two events were likely related, as suggested by the National Oceanic & Atmospheric Administration (NOAA)'s Space Environment Center (SEC) stratospheric warming alerts ([http://www.sec.noaa.gov/alerts/archive/alerts\\_Jan2003.html](http://www.sec.noaa.gov/alerts/archive/alerts_Jan2003.html)). Both warming events were accompanied by upper mesospheric coolings. For the second warming event, the upper mesospheric cooling also appeared to propagate downward (Fig. 3). Note that a similar correlation of stratospheric warmings and mesospheric coolings was observed with the TIMED/SABER instrument (Siskind et al., 2005; S. D. Eckermann, personal communication, 2005) and was modeled in several studies (Holton, 1983; Liu and Roble, 2002; Coy et al., 2005). The apparent link between stratospheric warmings and mesospheric coolings suggests important roles of planetary waves and GWs in stratosphere-mesosphere coupling (Holton, 1983; Liu and Roble, 2002; Coy et al., 2005; Siskind et al., 2005). During the warming on 15–17 January, winds were mostly to the northwest at 45–50 km and to the southeast in the upper mesosphere. Winds were very weak around 50 km and were mostly to the southeast in the upper mesosphere during the stratospheric warming on 24–27 January.

As noted in the previous section, the two FS salvos had a temporal resolution of  $\sim 1$  h. This made it possible to obtain

reliable estimates of the background fields and thus to derive GW perturbations. Figure 4 shows the salvo mean profiles, as well as individual soundings within each salvo. For both salvos, background winds were generally to the southeast in the stratosphere. In addition, winds were very weak at  $\sim 50$  km for Salvo 1. The background temperature profiles were very different between the two salvos. For Salvo 1, there was a temperature minimum at  $\sim 43$  km and a maximum at  $\sim 60$  km. For Salvo 2, however, the background temperature was roughly isothermal below  $\sim 55$  km and decreased monotonically above  $\sim 55$  km with a nearly adiabatic lapse rate. Compared with the reference atmosphere MSISE90 (Hedin, 1991) at  $70^\circ$  N in January (not shown), the background temperature during Salvo 1 was much colder than the reference temperature in the upper stratosphere (e.g., nearly 45 K colder at 42 km). The Salvo 2 background temperature was generally colder than the reference temperature by 10–15 K above 40 km, but its lapse rate agreed very well with the reference atmosphere.

Following the conventional approach, we derived GW perturbations by calculating the differences between raw soundings and the salvo means. Since the temporal coverage of each salvo was limited, namely  $\sim 12$  h for Salvo 1 and  $\sim 6$  h for Salvo 2, a high-pass (in wavenumber) filter with a cut-off wavelength of 18 km was applied to the differences to

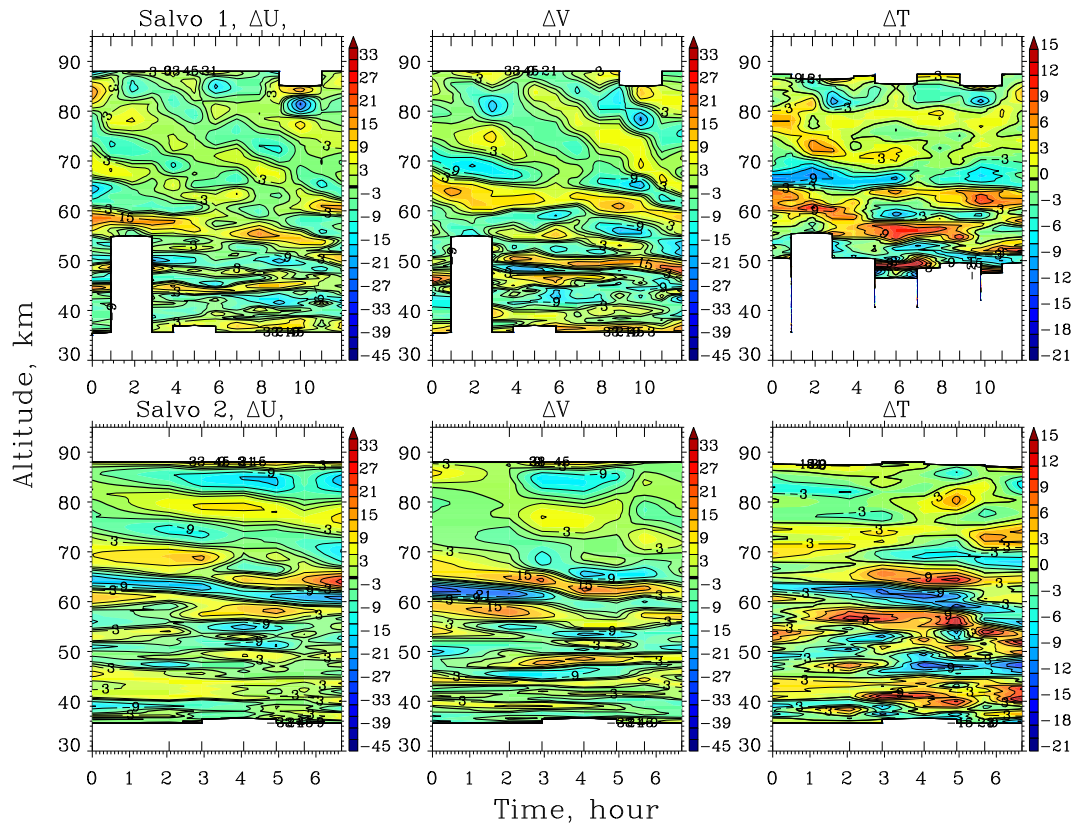


**Fig. 5.** Gravity wave perturbations for FS Salvo 1 and 2. The contour interval is  $2 \text{ ms}^{-1}$  for winds and 2 K for temperature. Times are relative to the first FS of each salvo, which were at 13:11 and 13:00 UTC, respectively.

minimize the possible contamination from planetary waves and semidiurnal tides, under the assumption that the vertical scales of those contaminants were longer than those of GWs in the altitude range considered. Figure 5 shows the time-altitude contours of GW perturbations thus derived for each salvo. Note that both velocity and temperature fields contain evidence of primarily downward phase progression, but also some upward phase progression, at higher altitudes. Upward phase progression can result from either downward energy propagation or Doppler shifting resulting in an observed phase speed opposite to, and larger than, the intrinsic phase speed. The latter appears to be the case here, since the hodograph analysis presented below indicates a clockwise rotation of the wind vector with altitude in all profiles. We also note that departures from linear relationships between the velocity and temperature fields can result from wave superposition, from instability dynamics, and are also observed in high-resolution lidar measurements exhibiting these same dynamics (Williams et al., 2006). For Salvo 1, the strongest GW perturbations occurred at 45–50 km, whereas for Salvo 2, the strongest GW perturbations occurred at  $\sim 60$  km, being consistent with the visual inspection of the raw soundings (Fig. 1). Finally, note that the apparent pattern

shown in Fig. 5 should be viewed with some caution, as the vertical resolution of FS data decreases with increasing altitude, thus waves with longer vertical wavelengths were removed with increasing height. Nevertheless, GW amplitudes generally increase with increasing altitude due to decreasing background atmospheric density, so the most energetic part of the GW spectrum was not impacted significantly by the observational selection factor.

For the balloon data, we first interpolated the raw data to a regular grid with a resolution of 50 m. We then derived GW perturbations in the lower stratosphere (above 11 km) by applying a high-pass (in wavenumber) filter with a cutoff wavelength of 5 km to each sounding. Some previous studies (e.g., Allen and Vincent, 1995; Wang and Geller, 2003; and Wang et al., 2005) derived GW perturbations by removing the mean profiles estimated from polynomial fits. It was found that the statistics of GW parameters such as horizontal propagation directions from the different estimates of GW perturbations were very similar. The lower stratospheric GW perturbations did not show any apparent phase propagation. The perturbation amplitudes were slightly larger at 20–30 km than at other altitude ranges (not shown).

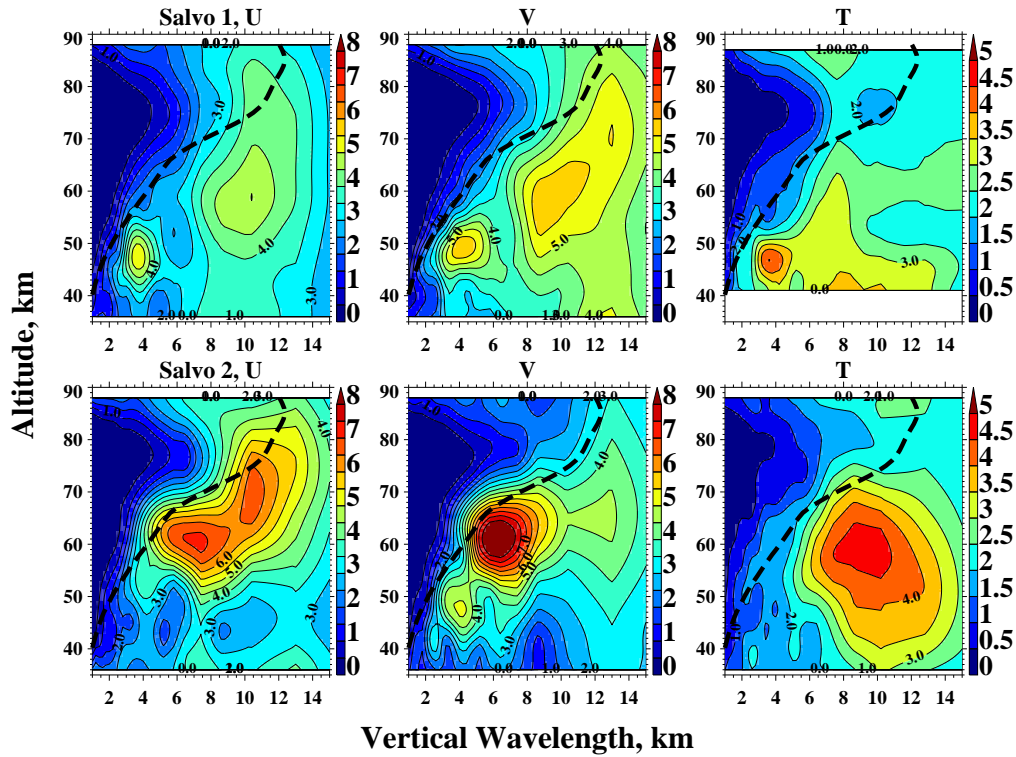


**Fig. 6.** Salvo mean vertical wavelength-altitude contours of S-transform amplitudes of FS winds and temperature. The dashed lines are the vertical profiles of the Nyquist vertical wavelength corresponding to the FS data. The contour interval is  $0.5 \text{ ms}^{-1}$  for winds and  $0.5 \text{ K}$  for temperature.

To show GW perturbation amplitudes and vertical scales quantitatively and more clearly, we applied the S-transform to each FS and balloon sounding to obtain contours of vertical scale vs. altitude of the perturbation amplitudes. The S-transform (e.g., Stockwell et al., 1996) is a Gaussian wavelet transform that is defined as a continuous wavelet transform (CWT) with a specific mother wavelet multiplied by the phase factor

$$S(\tau, f) = e^{i2\pi f\tau} W(\tau, d) \quad (1)$$

where  $\tau$  is time or altitude,  $f$  is frequency or vertical wavenumber, and the dilation factor  $d$  is the inverse of  $f$ . The CWT  $W(\tau, d)$  of a function  $h(t)$  is defined by

$$W(\tau, d) = \int_{-\infty}^{\infty} h(t)w(t - \tau, d)dt \quad (2)$$

and the mother wavelet  $w$  is defined as

$$w(t, f) = \frac{|f|}{\sqrt{2\pi}} e^{-\frac{t^2 f^2}{2}} e^{-i2\pi f t} \quad (3)$$

where  $t$  is also time or altitude. Writing out Eq. (1) explicitly gives the S-transform

$$S(\tau, f) = \frac{|f|}{\sqrt{2\pi}} \int_{-\infty}^{\infty} h(t) e^{-\frac{(t-\tau)^2 f^2}{2}} e^{-i2\pi f t} dt \quad (4)$$

The S-transform has been applied to geophysical data and has proven to be valuable in estimating GW amplitudes and phase information (e.g., Stockwell and Lowe, 2001; Wang et al., 2006).

Figure 6 shows the vertical wavelength-altitude contours of salvo mean S-transform amplitudes of FS zonal and meridional winds and temperature. Overplotted on the contour plots are the vertical profiles of the Nyquist vertical wavelength corresponding to the FS data (dashed lines). For Salvo 1, the principal maximum occurred at 45–50 km with a vertical scale of  $\sim 4$  km. There was a secondary maximum occurring at  $\sim 60$  km with a vertical scale of 9–10 km, especially in the wind data. For Salvo 2, the primary maximum of perturbations occurred at  $\sim 60$  km with a vertical scale of  $\sim 7$  km for wind components and 9–10 km for temperature. There was also an indication of weak GW enhancements for the meridional wind component at 45–50 km with a vertical scale of  $\sim 4$  km. Generally, GW perturbations were somewhat larger in Salvo 2 than in Salvo 1. The apparent very small amplitudes of short vertical scale GWs at high altitude were likely due to the observational selection factor of the FS data, although the dominant signals mentioned above were geophysical and were not affected significantly by the vertical resolution of the FS data. Note that much of the information displayed in Fig. 6 was already inferred from Figs. 1

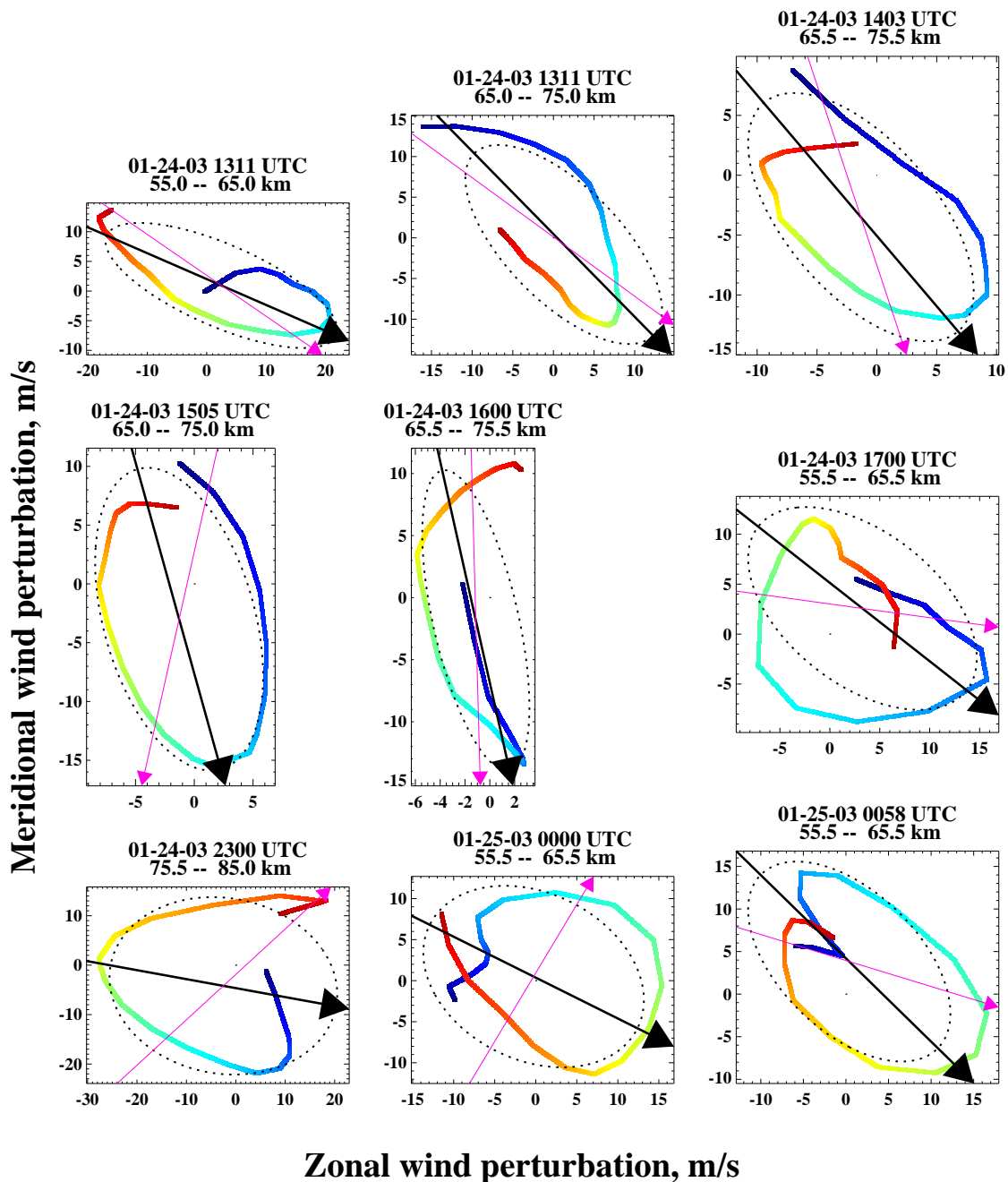


**Fig. 7.** Gravity wave perturbation hodographs (the thick colored lines) and the derived horizontal propagation directions for FS Salvo 1 at 60 km and above. The lowest altitude is denoted by blue color, whereas the highest altitude is denoted by red color. The thin dark dotted ellipse is the fit from the S-transform approach. The thick dark arrow denotes the direction estimated from the new approach. The thin pink arrow denotes the direction estimated from the Stokes parameter analysis. Ordering is chronological and then by increasing altitude. See text for details.

and 5, but Fig. 6 provides quantitative information regarding the locations, vertical scales, and amplitudes of the dominant wave motions. Note that the S-transform amplitudes of individual soundings within each salvo are generally similar to

one another (not shown) and they resemble the salvo mean patterns shown in Fig. 6. In the next section, GW parameters such as horizontal propagation direction will be derived for the dominant GW motions identified in Fig. 6.

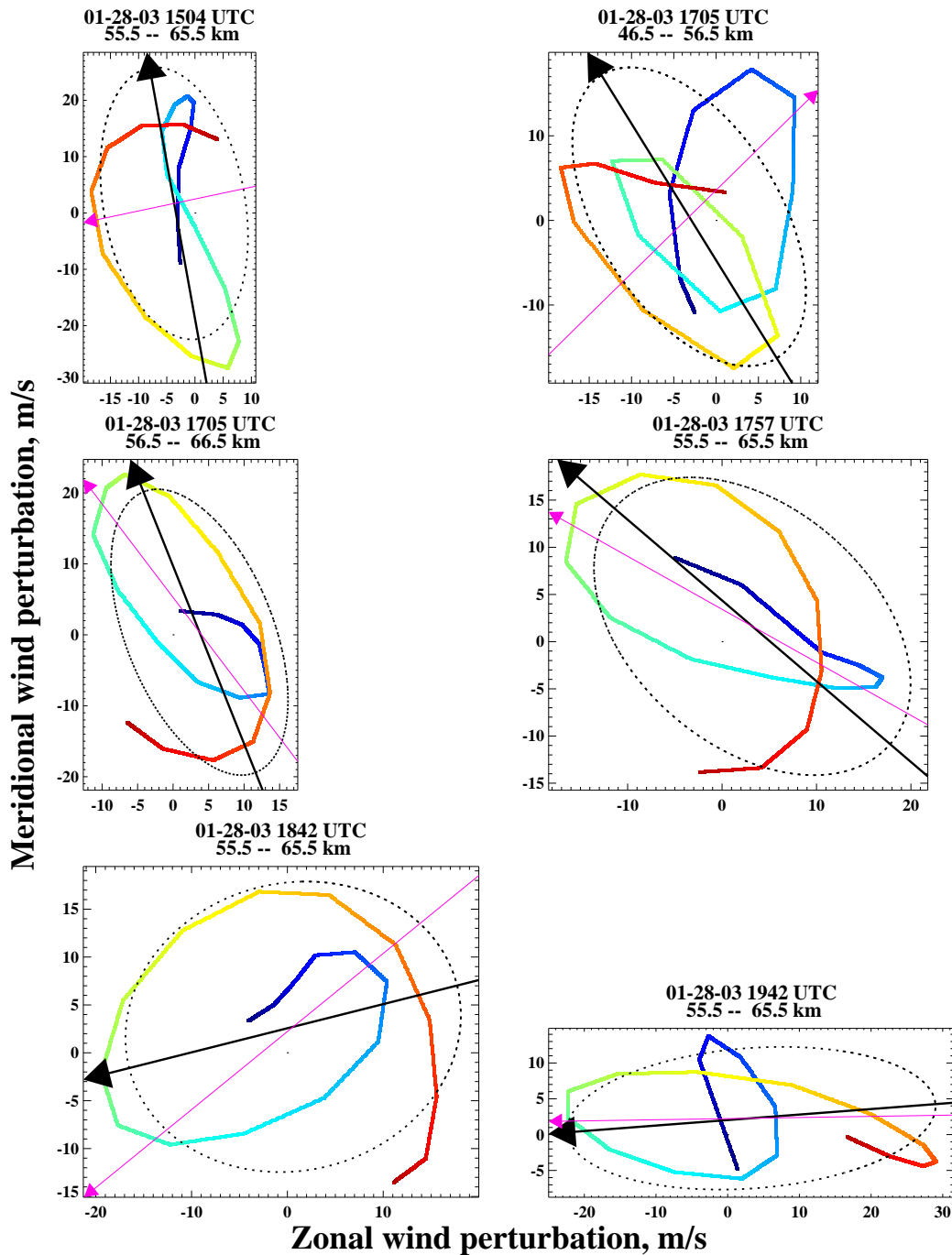


**Fig. 8.** Similar to Fig. 7 but for FS Salvo 2 at 60 km and above.

#### 4 GW Horizontal propagation directions

For a monochromatic GW propagating upward in the northern hemisphere, the wind perturbation hodograph depicts an ellipse rotating clockwise with increasing height. The orientation of the major axis of the ellipse is aligned with the horizontal propagation direction, and the ratio between the

lengths of the major and minor axes is equal to its intrinsic frequency divided by the Coriolis parameter. Linear GW theory also shows that the negative temperature perturbation lags the positive velocity perturbation in the direction of phase propagation by  $90^\circ$  (e.g., Gossard and Hooke, 1975). So, with vertical profiles of wind and temperature perturbations available, it is possible to determine GW horizontal

propagation directions and intrinsic frequencies if the perturbations are dominated locally by monochromatic waves. Different approaches have been used in previous studies to determine GW horizontal propagation direction. Several studies fitted the wind perturbation ellipse directly (e.g., Hirota and Niki, 1985), while others took a statistical approach by using the Stokes parameter analysis (e.g., Eckermann and Vincent, 1989; Vincent et al., 1997; Schöch et al., 2004; Williams et al., 2004). Realizing that vertical profiles often contain a mixture of GWs at different altitudes, Zink and Vincent (2001) used the Morlet wavelet to first identify isolated wave packets in radiosonde soundings and then used the Stokes method to analyze the isolated wave packets. Note that all the above techniques are inherently related, as shown in Eckermann (1996).

In this study, we introduce a new approach which is based on the traditional hodographic analysis combined with the S-transform method, and we compare the results from the new approach with the Stokes analysis. In essence, the new approach is a variation of the hodographic analysis. It takes advantage of the fact that the characteristics of the wind perturbation ellipse of a monochromatic GW, including the orientation of the major axis and the ratio between major and minor axes, depend only on the wave amplitudes of the zonal and meridional wind components, and the phase difference between them (see the Appendix). The S-transform has been shown to yield reliable estimates of wave amplitudes (Fig. 6). The phase difference between two variables can be calculated by performing a cross-S-transform analysis (cross ST) in analogy with cross-spectral analysis using the Fourier transform. The cross ST of two time series (or vertical profiles)  $h(t)$  and  $g(t)$  is defined as

$$S_h(\tau, f)\{S_g(\tau, f)\}^* \quad (5)$$

where  $\{S_g(\tau, f)\}^*$  is the complex conjugate of  $S_g(\tau, f)$ . The phase of the cross ST can be shown to be equivalent to the phase difference between  $g(t)$  and  $h(t)$ ,  $\Phi(\tau, f)_g - \Phi(\tau, f)_h$ . The 180° ambiguity in GW propagation direction is resolved using the relationship between the temperature and velocity perturbations along the major axis of the orbital ellipse.

In practice, for a given data segment, the location and vertical wavelength corresponding to the dominant wave motion were identified through the maximum S-transform amplitude of wind speed. The amplitudes of, and the phase differences between the zonal and meridional wind perturbations, were then used to determine the orientation of the wind perturbation ellipse and the intrinsic frequency, as described in detail in the Appendix. The direction of horizontal propagation was determined as described earlier in this section. With the vertical scale and intrinsic frequency known, other wave parameters such as horizontal wavelength, horizontal phase speed, etc., were determined using the GW dispersion relation.

Figure 7 shows wind perturbation hodographs from selected data segments for soundings in FS Salvo 1 at ~60 km

and above. The altitude range of each data segment was arbitrarily taken to be 10 km. These data segments were chosen because they correspond roughly to the secondary maximum identified in Fig. 6, and because they display well-defined wind perturbation ellipses, suggesting that the motions were dominated by monochromatic GWs. As the nature of the new approach suggests, it can only yield credible estimates of horizontal propagation directions for nearly monochromatic wave motions. The estimates of horizontal propagation directions from both the new approach and the Stokes analysis are indicated by different arrows in each plot. Generally, the results from the two approaches are consistent, i.e., GWs propagated predominantly towards the southeast. Figure 7 also suggests that the estimates using our new approach are considerably better than those from the Stokes analysis for some cases (i.e., they are closer to the orientations of the major axes of perturbation ellipses), notably the fourth and eighth data segments in Fig. 7.

Similarly, Fig. 8 shows selected wind perturbation hodographs and the estimated propagation directions for soundings in FS Salvo 2 at ~60 km and above. The selected data segments correspond to the primary GW perturbation maximum for Salvo 2 identified in Fig. 6. Again, the estimates of both approaches are generally consistent, but the new approach seems to yield better fits for some cases, notably the first data segment. It is interesting that GWs generally propagated towards the northwest or west in Salvo 2, i.e., nearly opposite to those in Salvo 1. The apparent better performance of the S-transform approach in estimating GW horizontal propagation directions in some cases, as shown in Figs. 7 and 8, is likely due to the capability of the S-transform to obtain more reliable estimates of wave amplitudes and phase differences.

Those GWs identified in Figs. 7 and 8 all had very low intrinsic frequencies ( $\hat{\omega}/f \sim 1.5-4$ ), as inferred from the aspect ratio of the ellipses. The hodographs in Figs. 7 and 8 also imply that GW vertical wavelengths in Salvo 2 at ~60 km were generally shorter than their counterparts in Salvo 1. The clockwise rotation of the hodographs suggests upward energy propagation, and downward phase propagation, consistent with what was seen in Figs. 1 and 5.

The primary GW perturbation maxima for FS Salvo 1 occurred at 45–50 km with vertical scales of ~4 km (Fig. 6). The corresponding hodographs in that altitude range shown in Fig. 9, however, are more complicated than those shown in Figs. 7 and 8, and generally do not reveal the well-defined ellipses, implying that there were likely a mixture of GWs. So, the new approach is not expected to obtain reliable estimates of GW properties in these cases. Nevertheless, the hodographs do exhibit some coherent structures, as will be discussed in detail in the next section. Compared with the hodographs at 60 km and above (Fig. 7), hodographs at 45–50 km for Salvo 1 (Fig. 9) generally show larger perturbation amplitudes, smaller vertical scales and higher intrinsic frequencies. In addition, the hodographs display a consistent

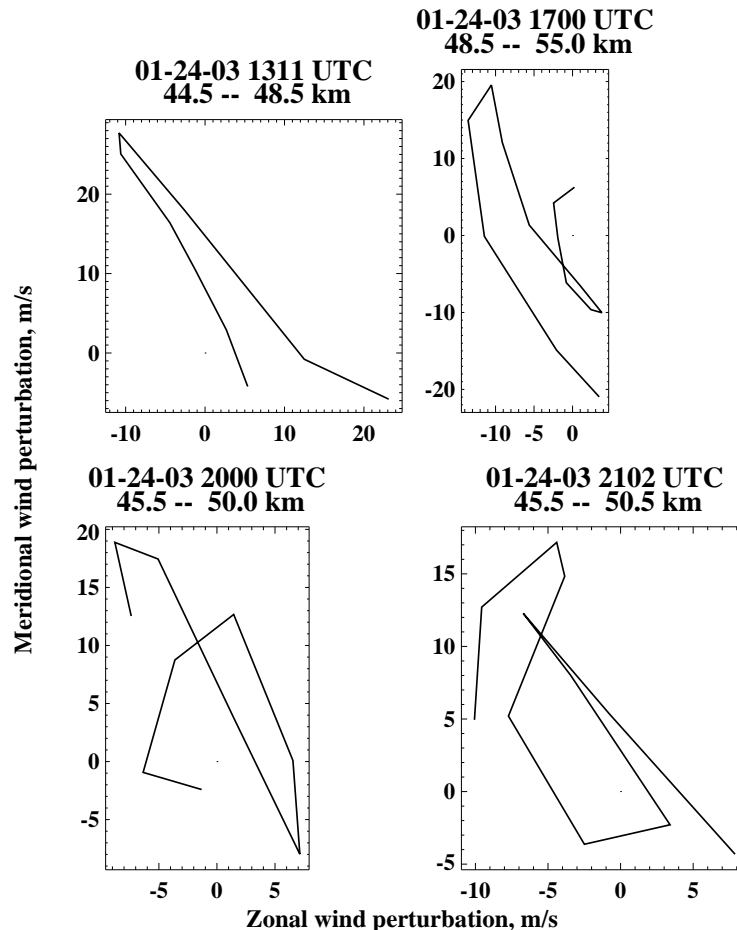


**Fig. 9.** Some of the gravity wave perturbation hodographs for FS Salvo 1 at around 45–50 km.

northwest-southeast orientation. Finally, it should be mentioned that the horizontal propagation directions in the lower stratosphere, as determined from the balloon data, were generally isotropic (not shown).

## 5 Discussion

GWs generally originate from sources in the lower atmosphere, and their major sources include topography, convection, and wind shear (Nastrom and Fritts, 1992; Fritts and Nastrom, 1992). As they propagate upward, they will be influenced significantly by the background winds and stability. In particular, a GW will typically break as it approaches its critical level. As a wave approaches its critical level, its vertical wavelength and vertical group velocity will approach zero. A topographic GW has a phase speed near zero, so its critical level exists where the background wind is close to zero in the direction of wave propagation.

Figure 10 shows the component of background wind in various directions for both salvos. The directions are measured counter-clockwise from the east. For example, a

northwest-southeast orientation corresponds to  $135^\circ$  in these plots. The wind vectors above 35 km were taken directly from the salvo mean winds, as shown in Fig. 4. The winds below 35 km were estimated from the average of the two balloon soundings over Esrange around the time of the respective salvos, as noted in Sect. 2. The averages were further smoothed using a 5-km low-pass filter before they were used to produce Fig. 10. The short gap in Salvo 1 was due to the relatively low balloon bursting altitudes during that period of time. Note that the wind measurements from the two instruments merged very well even though only two balloon soundings were available for each salvo.

It is evident that background winds were very weak in all directions at  $\sim 50$  km during Salvo 1, indicating the existence of a critical level at  $\sim 50$  km for mountain waves propagating in any direction. For Salvo 2, on the other hand, it is obvious that topographic waves could not reach the stratosphere due to the existence of critical levels in the troposphere. Additionally, the very low surface winds during Salvo 2 made it unlikely that mountain waves would be excited with any significant amplitude. These factors suggest

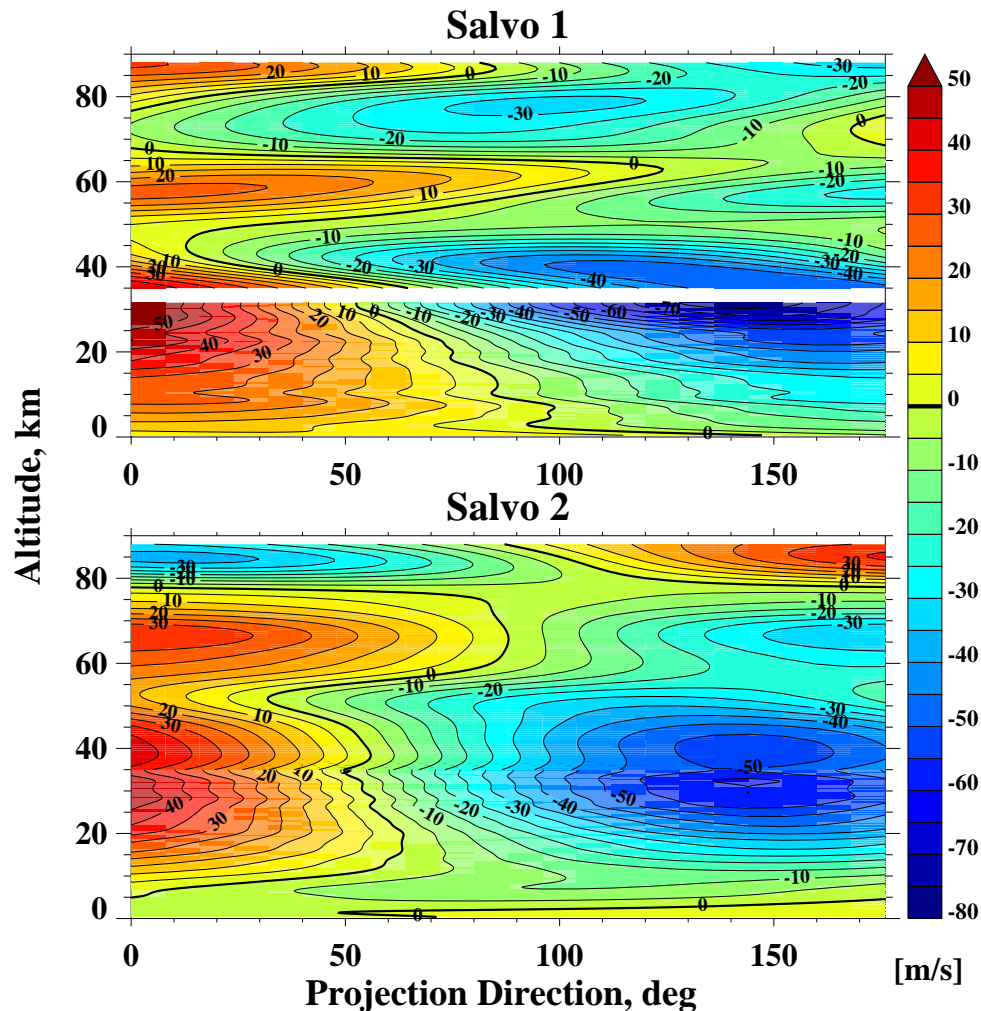


**Fig. 10.** Projection of salvo mean wind vectors on different directions ranging from 0 to 178°. The direction is measured counter clockwise from the East. The contour interval is  $5 \text{ ms}^{-1}$ . The zero wind line is marked by thick solid line. The blank region for Salvo 1 is due to a data gap. See text for details.

that the low-intrinsic-frequency GWs observed at 60 km and above for both Salvos 1 and 2 (Figs. 7 and 8) were not topographic waves. Also note that for Salvo 1, the background winds were mostly to the southeast below 50 km (Fig. 4), in the same direction as the wave propagation at 60 km and above (Fig. 7). One possible GW source was the strong wind shears near 20 km. They might also have come from sources well beyond Esrange due to the largely horizontal propagation of low-frequency GWs, though this was less likely since the propagation directions were so coherent within the salvo. It is unclear as to the exact source(s) of the waves for both Salvos 1 and 2 (except for the mountain waves in Salvo 1 as will be discussed later in this section) without more detailed analysis.

Figure 10 also indicates that there was likely selective transmission for topographic waves below 50 km depending on their propagation directions. More specifically, to-

pographic waves propagating in directions less than 100 deg or so (i.e., more or less towards the northeast or southwest) encountered critical levels well below 50 km. On the other hand, waves propagating in directions greater than 100 deg or so (or, more or less towards the northwest or southeast) could propagate throughout the stratosphere and lower mesosphere and encountered critical levels near 50 km. As has been observed in Fig. 9, wind perturbation hodographs for Salvo 1 at  $\sim 45\text{--}50$  km are aligned in a northwest-southeast orientation. This, together with the large perturbations and short vertical scales, suggests that the pronounced wave motions at 45–50 km for Salvo 1 were likely mountain waves approaching their critical levels.

Figure 11 shows vertical profiles of ratios of wind perturbation amplitudes and the corresponding intrinsic phase speeds (i.e.,  $u'_h/\hat{c}$ ), where  $u'_h$  is the wind speed amplitude) for the soundings in FS Salvo 1. The third sounding in the

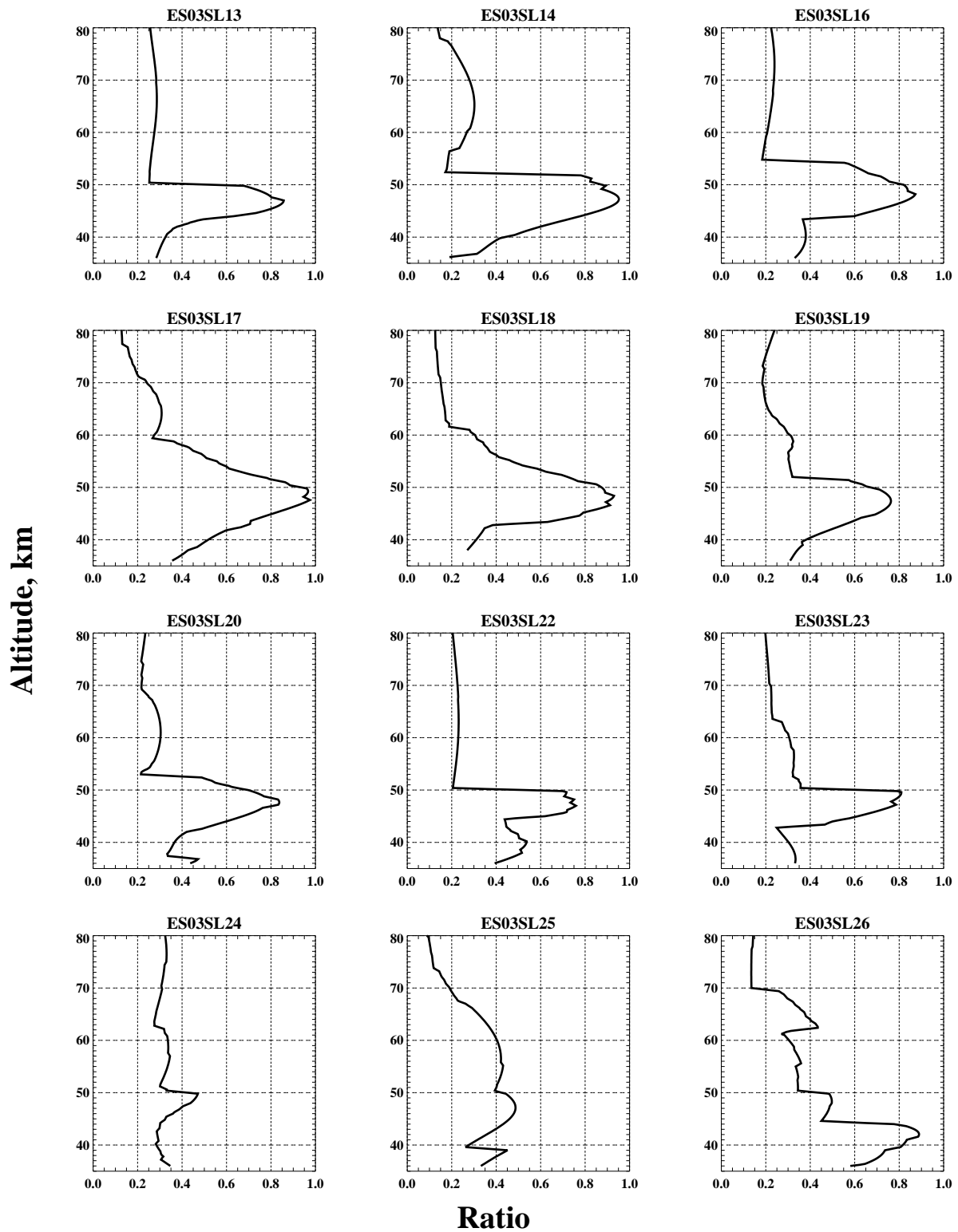


**Fig. 11.** Vertical profiles of the ratios of wind perturbation amplitude,  $u'/h$ , and intrinsic phase speed,  $\hat{c}$ , for the FS soundings in Salvo 1. The third sounding was excluded due to its limited vertical extent. The label on each plot is the sounding number. See text for further details.

salvo was excluded since there was a large vertical gap in the wind measurement (Fig. 1). This ratio indicates how close a GW is to being unstable. A value of 1 corresponds to a GW that is “convectively” unstable with  $d\theta/dz < 0$ , where  $\theta$  is total potential temperature (Fritts, 1984). In Fig. 11,  $u'_h$  was estimated from the maximum wind speed perturbation (which is related to the zonal and meridional components shown in Fig. 6 by  $u'_h = \sqrt{u'^2 + v'^2}$ ) at each altitude. The intrinsic phase speed was estimated from the corresponding vertical wavelength using the GW dispersion relation valid for medium intrinsic frequency waves,  $N \gg \hat{\omega} \gg f$ ,

$$|\hat{c}| = \frac{N\lambda_z}{2\pi} \quad (6)$$

where  $N$  is the buoyancy frequency calculated from the data,  $\hat{c}$  is the intrinsic phase speed, and  $\lambda_z$  is the vertical wavelength. It is remarkable that the ratios display sharp peaks at 45–50 km for nearly all of the soundings, and they decrease sharply above  $\sim 50$  km, which is the approximate critical level for topographic waves. The input to the calculation of the ratios shown in Fig. 11 includes  $u'_h$ , which achieved maxima at 45 to 50 km and were smaller below and above, and  $\hat{c}$ , which displayed minima at 45 to 50 km (not shown). Linear theory suggests that as a GW approaches its critical level, its amplitude will increase and its vertical scale will decrease, yielding a ratio  $u'_h/(\hat{c})$ , that likewise increases until dissipation occurs. Thus, Fig. 11 provides strong evidence that the large wind perturbations at 45–50 km with vertical wavelengths of  $\sim 4$  km, as shown in Fig. 6, were most likely topographic waves approaching their critical levels. The ratios for the last two soundings shown in Fig. 11 are different from the rest. These suggest that either mountain wave excitation was likely variable in time or that the critical level moved to a lower altitude (down to  $\sim 45$  km) during sounding number ES03SL26. The ratios approach, but do not reach, the threshold for convective instabilities, as expected from the linear theory. But this should not be surprising, given the recent numerical studies of GW breaking that demonstrated GW breaking for amplitude ratios less than 1 and amplitude reductions to values of  $\sim 0.3$  (Fritts et al., 2003, 2005).

## 6 Conclusions

Falling sphere and balloon wind and temperature measurements from the MaCWAVE winter campaign in January 2003 were analyzed to investigate GW characteristics in the stratosphere and mesosphere over northern Scandinavia.

The background was dominated by a minor stratospheric warming at  $\sim 30$  km on 24–27 January, which was accompanied by a downward-propagating upper mesospheric cooling during the same period. There was an earlier major stratospheric warming at  $\sim 45$  km during 17–19 January which was also accompanied by an upper mesospheric cooling.

Among the nearly three dozen FS soundings conducted during the winter campaign were two salvos which were

launched on 24–25 and 28 January, respectively. Within each salvo, the temporal resolution was  $\sim 1$  h, thus allowing for credible estimates of the mean fields and the extraction of GW perturbations for each sounding. GW perturbations for each sounding within each salvo were derived by removing the salvo mean field from the raw soundings which were then subjected to a high-pass filter to minimize the possible contamination of planetary waves and tides. The dominant GW perturbations for each sounding were identified using the S-transform, a Gaussian wavelet analysis. For soundings in Salvo 1, the strongest wave perturbations occurred at  $\sim 45$ – $50$  km with vertical wavelengths of  $\sim 4$  km. There was also a secondary maximum in GW amplitudes at  $\sim 60$  km with vertical wavelengths of  $\sim 9$ – $10$  km. For soundings in Salvo 2, the dominant wave amplitudes occurred at  $\sim 60$  km with vertical wavelengths of  $\sim 7$  km for winds and  $\sim 9$ – $10$  km for temperature.

A new approach, which is a variation of the conventional hodographic analysis, was introduced to estimate GW horizontal propagation directions for the dominant wave motions. Estimates from the new approach are generally consistent with the Stokes analysis, though the new approach seems to provide better estimates for some cases. For soundings in Salvo 1 at  $\sim 60$  km and above, GWs generally propagated towards the southeast, whereas for soundings in Salvo 2 in the same altitude range, GWs generally propagated towards the northwest or west. None of these waves could have been topographic waves due to the existence of mountain wave critical levels below 60 km. The source of the waves at these altitudes in Salvo 1 were mostly likely shear instability, likely at much lower altitudes.

The wind perturbation hodographs for soundings in Salvo 1 at  $\sim 45$ – $50$  km did not depict well-defined ellipses, indicating a possibility of mountain waves at higher intrinsic frequencies. Nevertheless, the hodographs suggested wave motions having short vertical wavelengths and large amplitudes, and they were aligned in a northwest-southeast orientation, which was within the selective transmission window for topographic waves to propagate upward until they encountered critical levels at  $\sim 50$  km. The ratios of perturbation amplitudes and intrinsic phase speeds for nearly all the soundings in Salvo 1 exhibited sharp peaks at 45–50 km and a remarkable reduction of these ratios just above 50 km. These results suggest that these GWs were most likely mountain waves approaching their critical levels.

Finally, we note that the new GW fitting approach estimating horizontal propagation directions only works when the perturbations are dominated by an individual GW. For future studies, it will be interesting to identify and reconstruct GW packets within a mixture of waves, as was done by Zink and Vincent (2001), and then to analyze the individual wave packets using the analysis method introduced in this study.

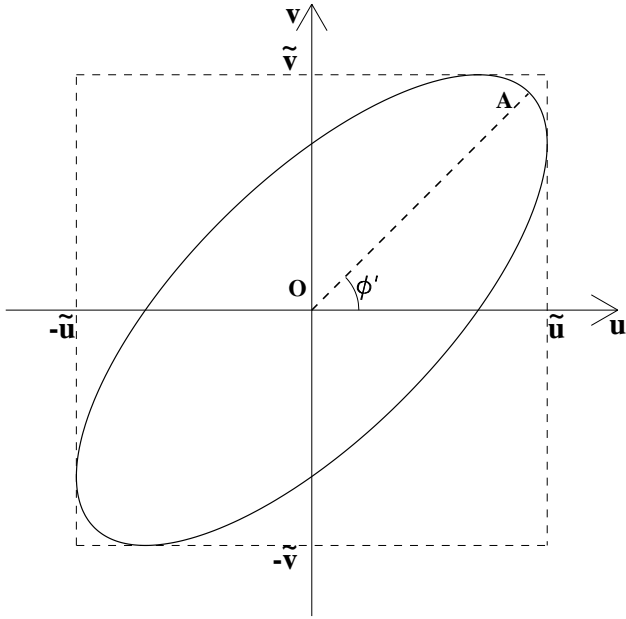


**Fig. A1.** Schematic of wind perturbation hodograph for a monochromatic gravity wave.

## Appendix A

### Determining hodograph ellipse from wind amplitudes and phase differences

For a monochromatic GW, the zonal and meridional wind components can be written as

$$u(z) = \tilde{u} \cos(mz) \quad (\text{A1})$$

$$v(z) = \tilde{v} \cos(mz + \Phi_0) \quad (\text{A2})$$

where  $\tilde{u}$  and  $\tilde{v}$  are the zonal and meridional wind amplitudes, respectively,  $m$  is the vertical wavenumber,  $z$  is altitude, and  $\Phi_0$  is the phase difference between  $u$  and  $v$ . The wind hodograph from Eqs. (A1) and (A2) forms an ellipse as illustrated in Fig. A1. The distance between a given point on the ellipse  $A$  and the origin  $O$  is

$$|AO| = \sqrt{\tilde{u}^2 \cos^2(mz) + \tilde{v}^2 \cos^2(mz + \Phi_0)} \quad (\text{A3})$$

The maximum and minimum distances of  $|AO|$  occur where  $d(|AO|)/dz=0$ , which leads to

$$2Bx^2 + Ax\sqrt{1-x^2} - B = 0 \quad (\text{A4})$$

where

$$x \equiv \cos(mz) \quad (\text{A5})$$

$$B \equiv \tilde{v}^2 \sin \Phi_0 \cos \Phi_0 \quad (\text{A6})$$

$$A \equiv \tilde{u}^2 + \tilde{v}^2 \cos^2 \Phi_0 - \tilde{v}^2 \sin^2 \Phi_0 \quad (\text{A7})$$

Equation (A4) can be solved numerically to determine the maximum and minimum values of  $|AO|$  which correspond to the lengths of the semi-major and semi-minor axes. Let  $x_0$  be the  $x$  corresponding to the maximum value of  $|AO|$ ,  $u_0 = \tilde{u}x_0$ , and  $v_0 = \tilde{v} \cos(\cos^{-1} x_0 + \Phi_0)$ , it can be shown that the orientation of the major axis of the ellipse  $\phi'$  is given by

$$\phi' = \cos^{-1}(u_0/\sqrt{u_0^2 + v_0^2}) \quad (\text{A8})$$

Note that the value of  $\phi'$  lies between 0 and  $\pi$ , whereas the propagation direction of the wave,  $\phi$ , ranges from 0 to  $2\pi$ . The temperature fluctuation can be used to solve the 180° ambiguity, as linear GW theory predicts that the (negative) temperature perturbation lags the (positive) wind perturbation along the propagation direction by 90°. The projection of  $(u, v)$  onto the orientation of the major axis of the ellipse  $AO$  is

$$u \cos \phi' + v \sin \phi' = C_1 \cos(mz + C_2) \quad (\text{A9})$$

where

$$C_1 =$$

$$\sqrt{(\tilde{u} \cos \phi' + \tilde{v} \sin \phi' \cos \Phi_0)^2 + (\tilde{v} \sin \phi' \cos \Phi_0)^2} \quad (\text{A10})$$

$$C_2 = \sin^{-1}(\tilde{v} \sin \phi' \sin \Phi_0 / C_1) \quad (\text{A11})$$

Let  $\Phi_T$  be the phase lag of temperature  $T$  with regard to  $u$ . The horizontal propagation direction  $\phi$  is  $\phi'$  if  $(\Phi_T - C_2)$  is within  $[0, \pi]$ , or  $\phi' + \pi$  if  $(\Phi_T - C_2)$  is within  $[\pi, 2\pi]$ . In practice, the S-transform is used to estimate wave amplitudes  $(\tilde{u}, \tilde{v})$ , and phase differences  $(\Phi_0, \Phi_T)$ .

*Acknowledgements.* The authors are grateful to M. J. Alexander, S. D. Eckermann, H.-L. Liu, and R. G. Stockwell for helpful discussions and comments on this study. We thank NILU for providing the ECMWF T106 data. The research was supported by NASA contract NAS5-02036, AFOSR contract F49620-03-C-0045, and NSF grant ATM-0137354. U. Blum is supported by the Marie-Curie Intra-European Fellowship program of the European Community (MINERWA, No 010333).

Topical Editor U.-P. Hoppe thanks P. Hoffmann and R. Vincent for their help in evaluating this paper.

## References

- Alexander, M. J., and Rosenlof, K. H.: Nonstationary gravity wave forcing of the stratospheric zonal mean wind, *J. Geophys. Res.*, 101, 23 465–23 474, 1996.
- Allen, S. and Vincent, R. A.: Gravity wave activity in the lower atmosphere: Seasonal and latitudinal variations, *J. Geophys. Res.*, 100, 1327–1350, 1995.
- Becker, E., Müllemann, A., Lübken, F.-J., Körnich, H., Hoffmann, P., and Rapp, M.: High Rossby-wave activity in austral winter 2002: modulation of the general circulation of the MLT during the MaCWAVE/MIDAS northern summer program, *Geophys. Res. Lett.*, 31, L24S03, doi:10.1029/2004GL019615, 2004.

- Becker, E. and Fritts, D. C.: Enhanced gravity-wave activity and interhemispheric coupling during the MaCWAVE/MIDAS northern summer program 2002, *Ann. Geophys.*, 24, this issue, 2006.
- Blum, U., Fricke, K. H., Müller, K. P., Siebert, J., and Baumgarten, G.: Long term lidar observations of polar stratospheric clouds at the Esrange in northern Sweden, *Tellus*, 57B, 412–422, 2005.
- Blum, U. and Fricke, K. H.: The Bonn University Lidar at the Esrange: Technical description and capabilities for atmospheric research, *Ann. Geophys.*, 23, 1645–1658, 2005.
- Blum, U., Baumgarten, G., Schöch, A., Kirkwood, S., Naujokat, B., and Fricke, K. H.: The meteorological background situation at polar latitudes during winter 2002/2003 in the context of the MaCWAVE campaign, *Ann. Geophys.*, 24, this issue, 2006.
- Coy, L., Siskind, D. E., Eckermann, S. E., McCormack, J. P., Allen, D. R., and Hogan, T. F.: Modeling the August 2002 minor warming event, *Geophys. Res. Lett.*, 32, doi:10.1029/2005GL022400, 2005.
- Dörnbrack, A., Birner, T., Fix, A., Flentje, H., Meister, A., Schmid, H., Browell, E. V., and Mahoney, M. J.: Evidence for inertia gravity waves forming polar stratospheric clouds over Scandinavia, *J. Geophys. Res.*, 107, doi:10.1029/2001JD000452, 2002.
- Dunkerton, T. J.: The role of gravity waves in the quasi-biennial oscillation, *J. Geophys. Res.*, 102, 26 053–26 076, 1997.
- Eckermann, S. D. and Vincent, R. A.: Falling sphere observations of anisotropic gravity wave motions in the upper stratosphere over Australia, *Pure Appl. Geophys.*, 130, 509–532, 1989.
- Eckermann, S. D.: Hodographic analysis of gravity waves: Relationships among Stokes parameters, rotary spectra, and cross-spectral methods, *J. Geophys. Res.*, 101, 19,169–19,174, 1996.
- Eckermann, S. D., Dörnbrack, A., Vosper, S. B., Flentje, H., Mahoney, M. J., Bui, T. P., and Carslaw, K. S.: Mountain wave-induced polar stratospheric cloud forecasts for aircraft science flights during SOLVE/THESEO 2000, *Wea. Forecasting*, in press, 2006.
- Fritts, D. C.: Gravity wave saturation in the middle atmosphere: a review of theory and observations. *Rev. Geophys.*, 22, 275–308, 1984.
- Fritts, D. C. and Nastrom, G. D.: Sources of mesoscale variability of gravity waves. part 2: frontal, convective, and jet stream excitation, *J. Atmos. Sci.*, 49, 111–127, 1992.
- Fritts, D. C. and Alexander, M. J.: Gravity wave dynamics and effects in the middle atmosphere, *Rev. Geophys.*, 41, 1003, doi:10.1029/2001RG000106, 2003.
- Fritts, D. C., Bizon, C., Werne, J. A., and Meyer, C. K.: Layering accompanying turbulence generation due to shear instability and gravity wave breaking, *J. Geophys. Res.*, 108, D8, 8452, doi:10.1029/2002JD002406, 2003.
- Fritts, D. C., Vadas, S. L., Wan, K., and Werne, J. A.: Mean and variable forcing of the middle atmosphere by gravity waves, *J. Atmos. Solar-Terres. Phys.*, in press, 2005.
- Goldberg, R. A., Fritts, D. C., Williams, B. P., Schmidlin, F. J., Croskey, C. L., Mitchell, J. D., Lübken, F.-J., Rapp, M., Singer, W., Latteck, R., Blix, T. A., Friedrich, M., Kirkwood, S., Mitchell, N., and Fricke, K. H.: The MaCWAVE program to study gravity wave forcing of the polar mesosphere during summer and winter, *ESA Symposium on European Rocket and Balloon Programmes and Related Research: 11th ESA Symposium*, Montreux, Switzerland, 24–28 May 1993, edited by: Kaldeich, B. and Rolfe, E. J., Eur. Space Agency, Paris, 345–350, 2003.
- Goldberg, R. A., Fritts, D. C., Williams, B. P., Lübken, F.-J., Rapp, M., Singer, W., Latteck, R., Hoffmann, P., Müllemann, A., Baumgarten, G., Schmidlin, F. J., She, C.-Y., and Krueger, D. A.: The MaCWAVE/MIDAS rocket and groundbased measurements of polar summer dynamics: Overview and mean state structure, *Geophys. Res. Lett.*, 31, L24S02, doi:10.1029/2004GL019411, 2004.
- Goldberg, R. A., Fritts, D. C., Schmidlin, F. J., Williams, B. P., Croskey, C. L., Mitchell, J. D., Friedrich, M., Russell III, J. M., Blum, U., and Fricke, K. H.: The MaCWAVE program to study gravity wave influences on the polar mesosphere, *Ann. Geophys.*, 24, this issue, 2006.
- Gossard, E. E. and Hooke, W. H.: *Waves in the Atmosphere*, Elsevier Science, New York, 1975.
- Hedin, A. E.: Neutral atmosphere empirical model from the surface to the lower exosphere MSISE90, *J. Geophys. Res.*, 96, 1159–1172, 1991.
- Hirota, I. and Niki, T.: A statistical study of inertia-gravity waves in the middle atmosphere. *J. Meteorol. Soc. Jpn.*, 63, 1055–1066, 1985.
- Hitchman, M. H., Gille, J. C., Rodgers, C. D., and Brasseur, G.: The separated polar winter stratopause: a gravity wave driven climatological feature, *J. Atmos. Sci.*, 46, 410–422, 1989.
- Hitchman, M. H., Bywaters, K. W., Fritts, D. C., Coy, L., Kudeki, E., and Surucu, F.: Mean winds and momentum fluxes over Jicamarca, Peru, during June and August 1978, *J. Atmos. Sci.*, 49, 2372–2383, 1992.
- Holton, J. R.: The role of gravity wave induced drag and diffusion in the momentum budget of the mesosphere, *J. Atmos. Sci.*, 39, 791–799, 1982.
- Holton, J. R.: The influence of gravity wave breaking on the general circulation of the middle atmosphere, *J. Atmos. Sci.*, 40, 2497–2507, 1983.
- Houghton, J. T.: The stratosphere and mesosphere, *Q. J. Roy. Meteor. Soc.*, 104, 1–29, 1978.
- Lindzen, R. S.: Turbulence and stress owing to gravity wave and tidal breakdown, *J. Geophys. Res.*, 86, 9707–9714, 1981.
- Liu, H.-L. and Roble, R. G.: A study of a self-generated stratospheric sudden warming and its mesospheric-lower thermospheric impacts using the coupled TIME-GCM/CCM3, *J. Geophys. Res.*, 107, doi:10.1029/2001JD001533, 2002.
- McFarlane, N. A.: The effect of orographically excited gravity wave drag on the general circulation of the lower stratosphere and troposphere, *J. Atmos. Sci.*, 44, 1775–1800, 1987.
- Mertens, C. J., Schmidlin, F. J., and Goldberg R. A., et al.: SABER observations of mesospheric temperatures and comparisons with falling sphere measurements taken during the 2002 summer MaCWAVE campaign, *Geophys. Res. Lett.*, 31, L03105, doi:10.1029/2003GL018605, 2004.
- Nastrom, G. D. and Fritts, D. C.: Sources of mesoscale variability of gravity waves. part 1: topographic excitation, *J. Atmos. Sci.*, 49, 101–110, 1992.
- Palmer, T. N., Shutts, G. J., and R. Swinbank: Alleviation of a systematic westerly bias in general circulation and numerical weather prediction models through an orographic gravity wave drag parameterization. *Q. J. R. Meteorol. Soc.*, 112, 1001–1039, 1986.
- Rapp, M., Strelnikov, B., Müllemann, A., Lübken, F.-J., and Fritts,

- D. C.: Turbulence measurements and implications for gravity wave dissipation during the MaCWAVE/MIDAS rocket program, *Geophys. Res. Lett.*, 31, L24S07, doi:10.1029/2003GL019325, 2004.
- Schmidlin, F. J., Lee, H. S., and Michel, W.: The inflatable sphere: a technique for the accurate measurement of middle atmosphere temperatures, *J. Geophys. Res.*, 96, 22 673–2 682, 1991.
- Schöch, A., Baumgarten, G., Fritts, D. C., Hoffmann, P., Serafimovich, A., Wang, L., Dalin, P., Mülleman, A., and Schmidlin, F. J.: Gravity waves in the troposphere and stratosphere during the MaCWAVE/ MIDAS summer rocket program, *Geophys. Res. Lett.*, 31, L24S04, doi:10.1029/2004GL019837, 2004.
- Siskind, D. E., Coy, L., and Espy, P.: Observations of stratospheric warmings and mesospheric coolings by the TIMED/SABER instrument, *Geophys. Res. Lett.*, 32, L09804, doi:10.1029/2005GL022399, 2005.
- Stockwell, R. G., Mansinha, L., and Lowe, R. P.: Localisation of the complex spectrum: the S transform, *J. Assoc. Expl. Geophys.*, XVII, 99–114, 1996.
- Stockwell, R. G. and Lowe, R. P.: Airglow imaging of gravity waves, 1. Results from a small network of OH nightglow scanning imagers, *J. Geophys. Res.*, 106, 17 185–17 203, 2001.
- Vincent, R. A., Allen, S. J., and Eckermann, S. D.: Gravity-wave parameters in the lower stratosphere. *Gravity Wave Processes: Their Parameterization in Global Climate Models*, edited by: Hamilton, K., Springer, 7–25, 1997.
- Wang, L. and Geller, M. A.: Morphology of gravity wave energy as observed from four years (1998–2001) of high vertical resolution U.S. radiosonde data, *J. Geophys. Res.*, 108, doi:10.1029/2002JD002786, 2003.
- Wang, L., Geller, M. A., and Alexander, M. J.: Spatial and temporal variations of gravity wave parameters, Part I: Intrinsic frequency, wavelength, and vertical propagation direction. *J. Atmos. Sci.*, 62, 125–142, 2005.
- Wang, L., Alexander, M. J., Bui, T. P., and Mahoney, M. J.: Small-scale gravity waves in ER-2 MMS/MTP wind and temperature measurements during CRYSTAL-FACE, *Atmos. Chem. Phys.*, 6, 1091–1104, 2006.
- Williams, B. P., Fritts, D. C., Wang, L., She, C. Y., Vance, J. D., Schmidlin, F. J., Goldberg, R. A., Müllemann, A., and Lübken, F.-J.: Gravity waves in the arctic mesosphere during the MaCWAVE/MIDAS summer rocket program, *Geophys. Res. Lett.*, 31, L24S05, doi:10.1029/2004GL020049, 2004.
- Williams, B. P., Fritts, D. C., She, C. Y., and Goldberg, R. A.: Gravity wave propagation through a large semidiurnal tidal and instabilities in the mesosphere and lower thermosphere during the winter 2003 MaCWAVE rocket campaign, *Ann. Geophys.*, 24, this issue, 2006.
- Zink, F. and Vincent, R. A.: Wavelet analysis of stratospheric gravity wave packets over Macquarie Island I. Wave parameters, *J. Geophys. Res.*, 106, 10 275–10 288, 2001.